

Microstructure.jl: a Julia Package for Probabilistic Microstructure Model Fitting with Diffusion MRI

Ting Gong^{1*}, Anastasia Yendiki¹

1 Martinos Center for Biomedical Imaging, Massachusetts General Hospital and Harvard Medical School, Charlestown, MA, United States

*Correspondence: tgong1@mgh.harvard.edu

Abstract: Microstructure.jl is a Julia package designed for probabilistic microstructure imaging using diffusion and combined diffusion-relaxometry MRI techniques. It provides a flexible and extendable framework for compartment models and includes robust and unified estimators for parameter fitting and uncertainty quantification. The package incorporates several established models from the literature, such as the spherical mean technique and soma and neurite density imaging (SANDI), along with their extensions for analyzing combined diffusion and T2 mapping data acquired at multiple echo times. For parameter estimation, it features methods like Markov Chain Monte Carlo (MCMC) sampling and Monte Carlo dropout with neural networks, which provide probabilistic estimates by approximating the posteriors of modelling parameters. Microstructure.jl is applicable to both in vivo and ex vivo imaging data. We are currently testing and optimizing the package and are pleased to share its major functionalities, design, and documentation progress.

Key words: microstructure, diffusion MRI, diffusion-relaxometry, Bayesian inference, Julia

1. Introduction

Microstructure imaging allows us to estimate biologically meaningful cellular parameters from MRI data, demonstrating high sensitivity and specificity in quantifying tissue morphology (Alexander et al., 2019; Novikov et al., 2019). This is achieved by parsimonious models that represent the tissue in a voxel as composed of a small set of compartments. Each tissue compartment corresponds to a different cellular structure, e.g., neurites or cell bodies, whose distinct geometry and composition gives rise to a different MR signal. Given data collected with an appropriate acquisition protocol, one can therefore disentangle the signals from these compartments and estimate their free parameters by solving an inverse problem. These parameters are informative on various tissue properties and can therefore serve as biomarkers for both healthy and diseased biological processes.

1.1 Challenges & Developments

MRI measurements are inherently noisy and exhibit varying sensitivities to different tissue features, posing significant challenges for parameter fitting, especially in complex models with higher-dimensional parameter spaces. Several issues complicate the parameter fitting process: **(1) Presence of local minima:** Non-linear objective functions defined on high-dimensional parameter spaces often have multiple local minima. As a result, optimization algorithms may converge on suboptimal solutions that are inaccurate estimates of the underlying tissue properties, and that are highly dependent on how the algorithm was initialized. **(2) Parameter degeneracy:** Different combinations of tissue parameters can produce similar MRI measurements, making it difficult to distinguish between them based on the data alone,

complicating the interpretation of fitted parameters. **(3) Lack of robustness:** Various factors, related to either experimental design or true individual variability, can degrade the accuracy of parameter estimates. On the one hand, MRI acquisition parameters, such as gradient strength or echo time (TE), affect the sensitivity of the measurements to specific tissue features, as well as image quality aspects such as signal-to-noise ratio (SNR) and artifacts. On the other hand, the heterogeneity of tissue properties across different regions or subjects can introduce estimation errors, if it is not modeled appropriately.

Maximum likelihood optimization methods, which provide a point estimate of parameters, are insufficient for quantifying and addressing these issues. For robust interpretation of the imaging measures, it is critical to provide estimates not only of the parameters of interest, but also of their uncertainty. Bayesian optimization methods allow uncertainty to be quantified by estimating the posterior distribution of parameters. This is also useful for identifying parameter degeneracy. For example, random sampling methods such as Markov Chain Monte Carlo (MCMC) generate samples drawn from the posterior distribution of the parameters (Gilks et al., 1995). These distributions capture the uncertainty around the estimate (Alexander, 2008; Behrens et al., 2003). The drawback of Bayesian methods is that they are computationally intensive, making them impractical for high-resolution, whole-brain datasets, and that they require tuning of the sampling parameters for each model.

Improving the speed and robustness of probabilistic microstructure model fitting is essential for making these models practical in large-scale neuroimaging studies. This involves a two-pronged approach: (i) leveraging high-performance languages and efficient computing to accelerate MCMC estimation methods and (ii) taking advantage of the recent developments in neural network-based estimation methods for even faster inference. Both MCMC and neural network-based approaches allow quantification of uncertainty in parameter estimates, and they may play complementary roles in managing the bias and variance trade-off of parameter estimation. Therefore, both methods are useful for addressing the challenges of microstructure imaging.

1.2 Microstructure models

Here, we introduce microstructure models briefly, to provide a common language for describing the features available in existing toolboxes and in Microstructure.jl.

Orientation-dependent models: These models consider the effects of fiber orientations to model signals and use either diffusion-weighted imaging (DWI) measurements with different gradient directions or their rotational invariant features as data points for model fitting (Alexander et al., 2010; Assaf and Basser, 2005; Behrens et al., 2003; Jespersen et al., 2010, 2007; Novikov et al., 2018; Zhang et al., 2012).

Orientation-averaged models: These models factor out the effects of fiber orientation through powder averaging (PA) (Callaghan et al., 1979) and focus on estimating other microstructure parameters. Thus, the inputs to microstructure model fitting are only PA signals obtained by averaging or fitting DWI measurements from different gradient directions at unique b-values and/or diffusion times. Examples include the spherical mean technique (Kaden et al., 2016), soma and neurite density imaging (SANDI) (Palombo et al., 2020), and several water exchange models (Jelescu et al., 2022; Olesen et al., 2022).

Combined diffusion-relaxometry models: These models extend those in the first two categories by introducing compartment-specific T2/T2* and/or T1 values as model parameters (Gong et al., 2023c, 2022, 2020; Lampinen et al., 2019; Slator et al., 2021; Veraart et al., 2017). They require DWI measurements to be collected at multiple echo times (TE) and/or inversion recovery times (TI). They may model fiber orientation explicitly or they may factor it out by PA. Combined diffusion-relaxometry models enable unbiased estimation of compartment fractions, which can otherwise be relaxation-weighted and protocol-dependent in the two previous categories of models. They also provide additional estimates of compartmental T2/T2*/T1 values that reflect the macromolecular environment of tissue compartments. While these models demand more extensive measurements and thus longer acquisition times, development of novel, efficient acquisition sequences (Dong et al., 2022; Fair et al., 2021; Hutter et al., 2018; Wang et al., 2019) and robust computation tools (de Almeida Martins et al., 2021; Gong et al., 2021a, 2021b; Palombo et al., 2023) is now making them practical for use in future studies.

1.3 Summary of existing software

MATLAB toolboxes. Several well-known toolboxes have made microstructure model fitting more accessible for basic and clinical neuroscience research. For example, the compartment modelling module in the UCL Camino Diffusion MRI Toolkit (Cook et al., 2005) implements a broad range of models, which have been described in a model comparison paper (Panagiotaki et al., 2012). These include models like ActiveAx for axon diameter estimation (Alexander et al., 2010) and VERDICT for cell size estimation (Panagiotaki et al., 2014). The NODDI toolbox, also from UCL, focuses on orientation-dispersed models for axon diameter (Zhang et al., 2011) and neurite density estimation (Tariq et al., 2016; Zhang et al., 2012). These MATLAB toolboxes are user-friendly tools for applying several models from the literature in research settings.

Python toolboxes. There are several Python toolboxes designed to provide consistent frameworks for parameter estimation across various microstructure models. The Microstructure Diffusion Toolbox (MDT) (Harms and Roebroeck, 2018) implements several orientation-dependent models and provides MCMC sampling methods for estimating parameters and quantifying uncertainty. It also supports GPU processing to speed up model fitting. Dmipy (Fick et al., 2019) is another python toolbox that implements a wide range of tissue compartments, including both orientation-distributed and spherical mean-based models, and provides several non-linear solvers for parameter estimation. In addition to MDT and Dmipy, the Amico toolbox (Daducci et al., 2015) implements several models from the literature, including ActiveAx, NODDI, and SANDI, with accelerated processing using linear approximations.

Other open-source tools. While not included in previous sections, some studies have shared code for implementing their microstructure models. For example, the SANDI toolbox (Palombo et al., 2020), the standard model imaging toolbox (Coelho et al., 2022) and qMRINet (Grussu et al., 2021) provide tools to fit specific models with machine learning. Other software tools, such as MRtrix (Tournier et al., 2019) and Dipy (Garyfallidis et al., 2014), focus primarily on signal models for fiber orientation estimation and tractography.

1.4 Features of Microstructure.jl

Microstructure.jl aims to provide a flexible and probabilistic framework for microstructure model fitting, leveraging the intuitive and high-performance language Julia (Bezanson et al., 2014). It is designed not

only as an application tool with a user-friendly interface but also as a developer tool that can be easily extended. Compared to existing toolboxes, it has a unique combination of features: 1. Support for combined diffusion-relaxometry modelling; 2. Generic MCMC and neural network estimators for parameter estimation and uncertainty quantification, in which model fitting assumptions can be easily adjusted. 3. Compatibility with other probabilistic programming libraries in the Julia ecosystem, such as Turing. Currently, Microstructure.jl includes spherical-mean based models for microstructure imaging. In parallel, we are developing a companion Julia package, Fibers.jl, for fiber orientation estimation and tractography.

In the following sections, we describe the main functionality and structure (section 2) and demonstrate key use cases (section 3). Microstructure.jl can be installed through Julia's built-in package manager. Source code is available at: <https://github.com/Tinggong/Microstructure.jl>. Documentation, including full API manuals and tutorials, is available at: <https://tinggong.github.io/Microstructure.jl/dev/>.

2. Package design

Figure 1 demonstrates an overview of the relationships between major data types and functions in Microstructure.jl. We introduce each module in detail in the following.

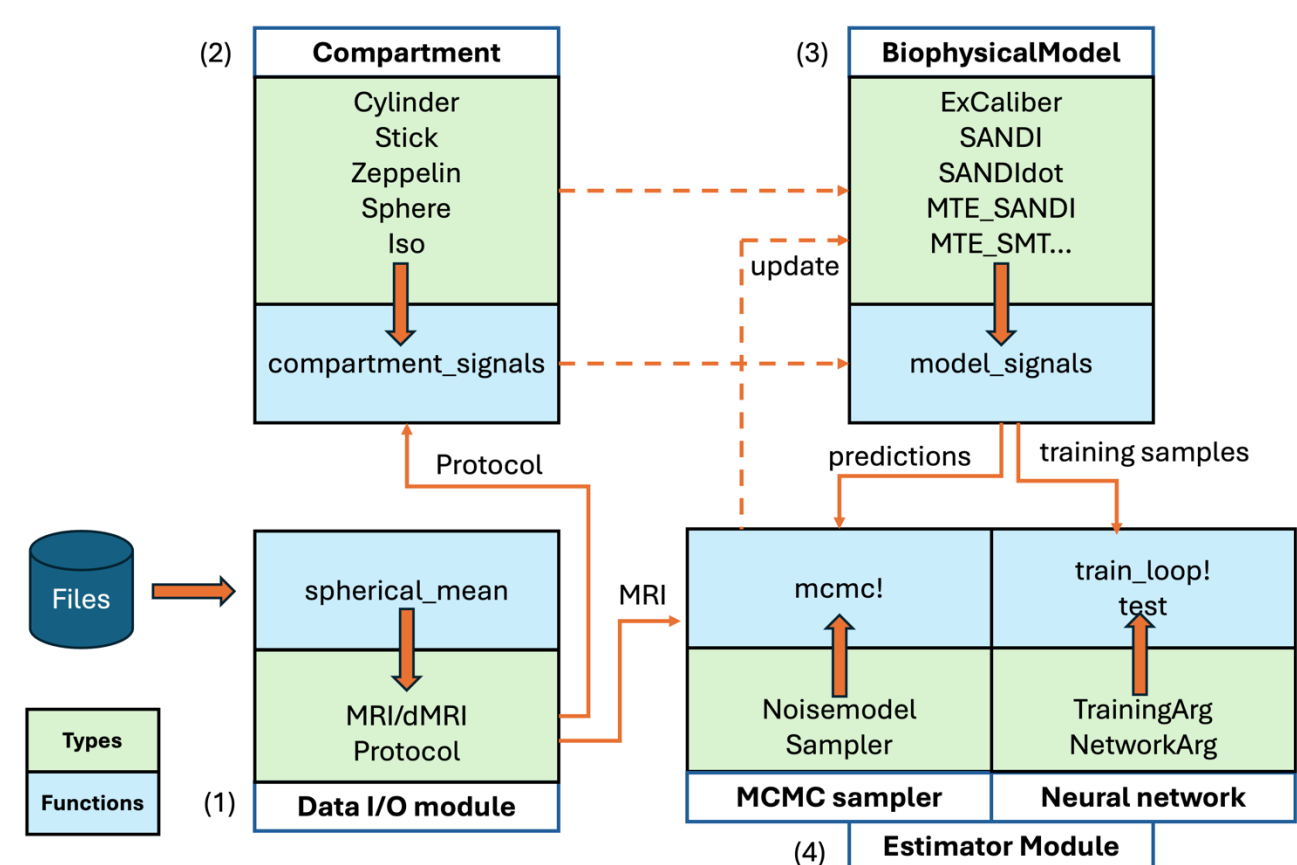


Figure 1. Package overview. The diagram shows the main data types (green boxes) and functions (blue boxes) in each module of Microstructure.jl. The direction of the orange arrow between a green and blue box indicates if a certain type is an input or output to the respective function.

2.1 Data IO

In the IO module, Microstructure.jl handles reading DWI volumes and text files with acquisition parameters to prepare the input data and protocols necessary for microstructure parameter fitting. The module includes functions to read DWI measurements from NIfTI or Bruker image files (via calls to the Fibers.jl package) and to perform gradient direction averaging for different b-values, TEs, diffusion gradient duration and separation times. These functions return an MRI-type structure containing the spherical mean signals and an image protocol type structure that includes fields necessary for advanced microstructure modelling.

2.2 Tissue Compartments

In Microstructure.jl, tissue compartments are implemented as composite types, with fields that store relevant tissue microstructure parameters. The function ‘*compartment_signals*’ predicts the normalized spherical mean signals (Callaghan et al., 1979; Kaden et al., 2016; Kroenke et al., 2004) given a tissue compartment object and an imaging protocol. The multiple dispatch in Julia is used to flexibly implement different methods (meaning the forward model) based on the compartment type. When specified, compartmental T2 values are included in the forward model, as demonstrated in previous works (Gong et al., 2023c, 2020; Lampinen et al., 2019; Veraart et al., 2017) for combined diffusion-relaxometry imaging. Currently, 5 different compartments are included in the package. Their parameters and formular are given below. While all relevant parameters are given for each compartment, this does not mean that they can all be estimated robustly. The decision about which parameters to estimate is made based on settings in the estimators.

Zeppelin. The zeppelin model is a tensor with equal water diffusivity in the two perpendicular directions, which is expected to be smaller than the water diffusivity in the parallel direction. This compartment is usually used to represent an anisotropic extra-cellular environment typically seen in the white matter (WM) (Alexander, 2008; Jespersen et al., 2010). The normalized signal follows the spherical mean expression as:

$$S_{\text{zeppelin}}(b(\delta, \Delta, G), t; D_{\parallel}, D_{\perp}, T_2) = e^{-t/T_2} e^{-bD_{\perp}} \sqrt{\frac{\pi}{4b(D_{\parallel}-D_{\perp})}} \operatorname{erf}(\sqrt{b(D_{\parallel}-D_{\perp})}) \quad [1],$$

where the three free parameters D_{\parallel} , D_{\perp} and T_2 are the parallel diffusivity, perpendicular diffusivity and the T2 value of water within the Zeppelin compartment; $\operatorname{erf}(\cdot)$ is the error function; b is the diffusion gradient weighting b-value that can be computed from the diffusion gradient duration times δ , separation times Δ and strengths G , as $b = \gamma^2 G^2 \delta^2 (\Delta - \delta/3)$ for a pulsed gradient spin echo encoding; and t is the TE.

The signals measured at N sets of protocol variables b and t constitute signal vector $\mathbf{S} = [S_{\text{zeppelin}}^1, \dots, S_{\text{zeppelin}}^N]$, where $S_{\text{zeppelin}}^i = S_{\text{zeppelin}}(b_i(\delta_i, \Delta_i, G_i), t_i; D_{\parallel}, D_{\perp}, T_2)$ and $i = 1, \dots, N$. The relaxation weighting term e^{-t/T_2} in Eq [1] is included in the signal vector \mathbf{S} if multi-TE data (i.e. different t_i values) are provided for combined diffusion-relaxometry imaging, which is otherwise ignored for conventional microstructure imaging. The definition of protocol variables b and t , and inclusion of relaxation-weighting in signal vector \mathbf{S} are the same for all the compartments below and thus are not repeated in the following.

Cylinder. In the cylinder model, water diffusion in the perpendicular direction in Eq [1] is related to the cylinder diameter through the Gaussian phase distribution (GPD) approximation. (Andersson et al., 2022; Fan et al., 2020; Van Gelderen et al., 1994). This compartment is used to represent axons when the imaging acquisition protocol can provide sensitivity to the axon diameter. Therefore, the normalized signal is:

$$S_{cylinder}(b(\delta, \Delta, G), t; D_{\parallel}, D_0, d_a, T_2) = e^{-t/T_2} e^{-bD_{\perp}} \sqrt{\frac{\pi}{4b(D_{\parallel}-D_{\perp})}} \operatorname{erf}(\sqrt{b(D_{\parallel}-D_{\perp})});$$

And $-bD_{\perp} =$

$$-2\gamma^2 G^2 \sum_{m=1}^{\infty} \frac{1}{D_0^2 \alpha_m^6 (r_a^2 \alpha_m^2 - 1)} (2D_0 \alpha_m^2 \delta - 2 + 2e^{-D_0 \alpha_m^2 \delta} + 2e^{-D_0 \alpha_m^2 \Delta} - e^{-D_0 \alpha_m^2 (\Delta-\delta)} - e^{-D_0 \alpha_m^2 (\Delta+\delta)}) [2],$$

where the four free parameters D_{\parallel} , D_0 , d_a and T_2 are the parallel diffusivity, intrinsic diffusivity, cylinder diameter and T2 value, respectively; $r_a = d_a/2$ is the cylinder radius; α_m is the m -th root of $J'_1(\alpha r_a) = 0$ and J'_1 is the derivative of the first-order Bessel function of the first kind.

Stick. When the imaging protocol is not sensitive to axon diameter, a stick model is used to represent the axons (Behrens et al., 2003), where the water diffusivity perpendicular to the axons is approximately zero, therefore the normalized signal is given by:

$$S_{stick}(b(\delta, \Delta, G), t; D_{\parallel}, T_2) = e^{-t/T_2} \sqrt{\frac{\pi}{4bD_{\parallel}}} \operatorname{erf}(\sqrt{bD_{\parallel}}) [3],$$

where the two free parameters D_{\parallel} and T_2 and the parallel diffusivity and T2 values of water, respectively, in the stick compartment. This compartment is used for estimating the intra-neurite signal fraction and diffusivity with lower b-value acquisition protocols.

Sphere. The sphere model is an isotropic compartment where diffusion of water molecules is assumed to be restricted in spheres of radius r_a . This compartment is used to represent cell bodies more abundant in the gray matter (GM) (Palombo et al., 2020). The normalized signals given by GPD is (Balinov et al., 1993; Neuman, 1974):

$$S_{sphere}(b(\delta, \Delta, G), t; D_{is}, r_s, T_2) = e^{-t/T_2} e^{\{-2\gamma^2 G^2 \sum_{m=1}^{\infty} \frac{1}{D_{is}^2 \alpha_m^6 (r_s^2 \alpha_m^2 - 1)} (2D_{is} \alpha_m^2 \delta - 2 + 2e^{-D_{is} \alpha_m^2 \delta} + 2e^{-D_{is} \alpha_m^2 \Delta} - e^{-D_{is} \alpha_m^2 (\Delta-\delta)} - e^{-D_{is} \alpha_m^2 (\Delta+\delta)})\}} [4],$$

where the three free parameters D_{is} , r_s , and T_2 are the water diffusivity, radius, and T2 value, respectively, in the sphere compartment; α_m is the m -th root of $\frac{1}{\alpha r_s} J_{\frac{3}{2}}(\alpha r_s) = J_{\frac{5}{2}}(\alpha r_s)$ and J_n is the Bessel function of the first kind.

Iso. This compartment is used to model tissue environments in which water exhibits isotropic Gaussian diffusion. Its normalized signals are thus given by:

$$S_{iso}(b(\delta, \Delta, G), t; D, T_2) = e^{-t/T_2} e^{-bD} [5],$$

where the free parameters D and T_2 are diffusivity and T2 value of water, respectively, in the compartment. An isotropic compartment can be used to model: (i) cerebrospinal fluid (CSF), where D is free water diffusivity, usually fixed to $3 \mu\text{m}^2/\text{ms}$ for in vivo tissue and $2 \mu\text{m}^2/\text{ms}$ for ex vivo tissue; (ii) the

extra-cellular compartment, where D is dependent on the tissue environment and estimated from the data; or (iii) immobile water in ex vivo tissue, where the diffusivity D is set to 0.

2.3 Biophysical Models

A biophysical model for microstructure imaging is a combination of multiple compartments to represent the signals measured in a tissue voxel. In Microstructure.jl, water exchange between compartments is currently not considered; therefore, one should consider whether the experimental regime is appropriate for this assumption. This section introduces examples specific to modelling WM and GM tissue.

GM models. The package includes the SANDI model (Palombo et al., 2020) and its extensions for GM microstructure imaging. The ‘SANDI’ model is a three-compartment model, where cell soma, neurite, and extra-cellular space are modelled as Sphere, Stick, and Iso compartments, respectively. For ex vivo imaging, the ‘SANDIdot’ model includes an additional “dot” compartment (Iso compartment with diffusivity equal to 0) to account for immobile water in ex vivo tissue (Olesen et al., 2022). We have used this model to study cellular changes due to brain development in ex vivo macaque brain samples from early infancy to adulthood (Gong et al., 2024a). Lastly, the ‘MTE_SANDI’ model supports data collected with multiple echo times and can also estimate the T2 values in the soma, neurite, and extra-cellular compartments (Gong et al., 2023c).

WM models. The package includes two types of WM models. The first type models the axonal space as a Cylinder compartment and assumes that the data were acquired with strong enough diffusion gradients to be sensitive to the size of axons (Andersson et al., 2022; Fan et al., 2020). The ‘ExCaliber’ model is one example, where axon space is modelled as a Cylinder compartment, extra-cellular space modelled as a Zeppelin compartment, and an Iso compartment is used either with diffusivity equal to zero, to represent immobile water when imaging ex vivo tissue (Gong et al., 2024a, 2023a) or with diffusivity equal to that of free water, to represent CSF when imaging in vivo tissue (Fan et al., 2020). The second type of WM model represents axons as a Stick compartment and is applicable to data acquired on clinical systems (Kaden et al., 2016). ‘MTE_SMT’ is such a model, with Stick and Zeppelin compartments that have distinct compartmental T2 values.

2.4 Estimators

Estimators in Microstructure.jl provide flexible settings to determine which parameters of a biophysical model will be estimated and how. Given that not all free parameters in a model can be estimated robustly from the available data, this flexibility allows for the evaluation and adjustment of model fitting assumptions.

MCMC. Microstructure.jl implements the Metropolis-Hastings sampling algorithm without relying on external sampling libraries. It provides flexible arguments through the ‘Sampler’ and ‘Noisemodel’ inputs, allowing the user to apply the estimator to sample any parameters from any biophysical model. It is also possible to apply other advanced MCMC sampling methods to models in Microstructure.jl with Turing.jl (<https://turinglang.org/>), a general-purpose library for Bayesian inference. Initial evaluations indicate that Turing.jl sampling is slower than the native MCMC implementation in Microstructure.jl, and more

detailed testing will be conducted in the future. To accelerate MCMC sampling for large datasets, Microstructure.jl supports multi-thread processing.

MC dropout with neural networks. Microstructure.jl includes multi-layer perceptron (MLP) models for supervised training, utilizing dropout during inference to approximate posterior distributions. This module uses the machine learning library Flux.jl (<https://fluxml.ai/>) and allows flexible parameterization of MLPs through “NetworkArg” and training options through “TrainingArg”. While simple network architectures can be effective for microstructure fitting, the accuracy and generalizability of trained network models is highly dependent on the training datasets. For example, training samples generated from parameter fittings of brain datasets can introduce unbalanced prior distributions of the parameters in the training samples; and that can introduce bias to estimates particularly in regions where the true parameter values are underrepresented (Li et al., 2019).

Table 1 and Table 2 in the appendix include brief explanations of the arguments of the MCMC and neural network estimators. More detailed information can be found in our API manuals on the documentation website. Ongoing efforts for optimization of estimators are summarized in section 4.

3. Demonstrations

We demonstrate example applications of Microstructure.jl for protocol design and assessment; evaluation and adjustment of modelling assumptions; and evaluation of estimation accuracy and precision for an axon diameter estimation model for ex vivo tissue. These demonstrations highlight the importance of having an easy-to-use package for optimizing data acquisition and parameter fitting for microstructure imaging.

3.1 Protocol design for axon diameter estimation

When estimating axon diameter indices from MRI data, the sensitivity range of such estimates is closely associated with experimental factors, such as gradient strength and diffusion times, and tissue properties such as the intrinsic diffusivity. Therefore, evaluation of experimental settings is important for understanding the validity of the axon diameter index. Following the sensitivity criterion for the PA signal introduced by previous studies (Andersson et al., 2022; Nilsson et al., 2017), we can conveniently calculate the sensitivity range of axon diameter index estimates obtained from Microstructure.jl.

The sensitivity criterion concerns whether the normalized signal along a single gradient can be differentiated from the noise floor and the maximum signal. The smallest measurable signal attenuation $\bar{\sigma}$ relates to the SNR level of the signal as follows:

$$\bar{\sigma} = \frac{z_\alpha}{SNR\sqrt{n}},$$

where n is the number of measurements and z_α is the z-threshold for the significance level α ($z_\alpha = 1.64$ when $\alpha = 0.05$). The PA signal from a Cylinder compartment is upper bounded by a Cylinder with zero diameter, which is equal to the Stick model signal. A Cylinder therefore has a measurable diameter if its PA signal falls within the range of $[\bar{\sigma}, S_{stick} - \bar{\sigma}]$. Given a single b-value, the lower and upper bounds of axon diameter are thus the minimal diameter that gives $S_{cylinder}$ smaller than $S_{stick} - \bar{\sigma}$ and maximal diameter that gives $S_{cylinder}$ above $\bar{\sigma}$.

Sensitivity range for single high b-value. Using this criterion, we calculate the sensitivity ranges of axon diameter estimation at different high b-values feasible on a 4.7 T preclinical scanner with maximum gradient strength $G_{max} = 660$ mT/m. We investigate the effects of diffusion time and b-value to sensitivity ranges by using different diffusion times that reach the G_{max} with different b-values. We assume that the number of gradient directions is 32 and the ex vivo intrinsic diffusivity is $0.6 \mu\text{m}^2/\text{ms}$. We consider SNR levels of 100, 50 and 30.

Given same diffusion times in each plot, the sensitivity ranges shift towards smaller axons when the gradient strength G and thus b-value increases, as seen in Figure 2(A-C). Higher gradient strengths yield sensitivity to smaller axons, which are most abundant in tissue. However, they also reduce the sensitivity to very large axons, e.g. axons with diameter $> 7.5 \mu\text{m}$ for $G = 660$ mT/m. Given the same gradient strength G , shorter diffusion times and therefore lower b-value widens the sensitivity range on both sides. For example, see $G \approx 660$ mT/m, $b = 25, 43$ and 64 in Figure 2(A-C). Given the same b-value, shorter diffusion time and thus higher G lowers the lower bound of axon diameters that can be estimated accurately, but also reduces sensitivity to larger axons. This analysis suggests that using higher gradient strength and shorter diffusion time to achieve lower b-value is preferable, as it achieves a wider sensitivity range that covers most axon diameters expected in real tissue.

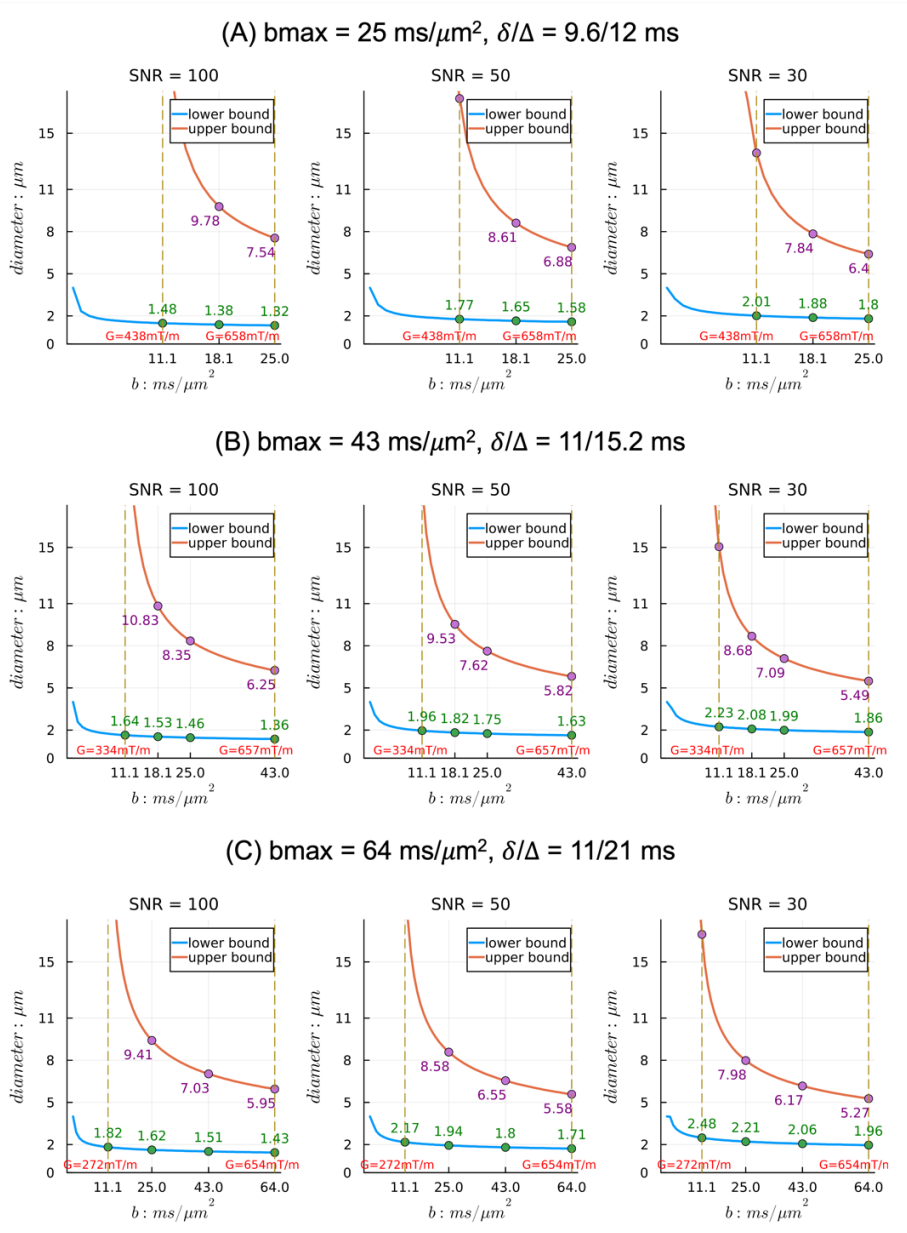


Figure 2. Sensitivity ranges of axon diameter index with single b -value data from the Cylinder model assuming $D_0 = 0.6 \mu\text{m}^2/\text{ms}$, $n = 32$ directions, and different SNR levels. Different diffusion times (A-C) are considered to achieve different b -values with $G_{\max} \approx 660 \text{ mT}/\text{m}$.

Comparison to in vivo sensitivity ranges. We can also assess the effects of the intrinsic diffusivity of tissue on the sensitivity range. We consider diffusivities typical of ex vivo brain ($D_0 = 0.6 \mu\text{m}^2/\text{ms}$) and in vivo brain ($D_0 = 1.7 \mu\text{m}^2/\text{ms}$). We include acquisition parameters relevant for in vivo human imaging with strong gradients ($b = 9 \text{ ms}/\mu\text{m}^2$, $G \sim 300 \text{ mT}/\text{m}$), in addition to the acquisition parameters relevant to ex vivo imaging that were detailed above. Results are shown in Figure 2(B). The lower diffusivity plays a critical role in the lower resolution limits in ex vivo tissue.

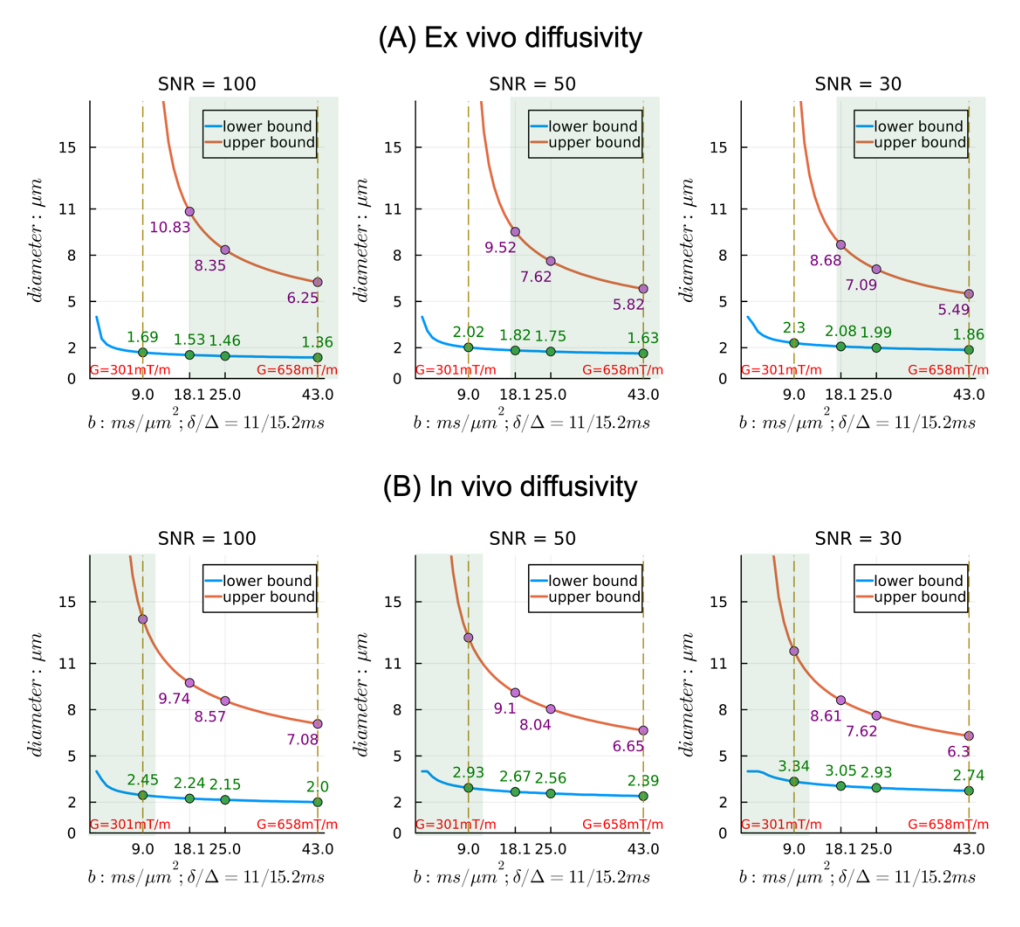


Figure 3. Sensitivity ranges for axon diameter estimation in ex vivo (A, $D_0=0.6 \mu\text{m}^2/\text{ms}$) and in vivo (B, $D_0 = 1.7 \mu\text{m}^2/\text{ms}$) brain tissue with single b-value data from the Cylinder model, assuming $n = 32$ directions and different SNR levels.

Sensitivity range for multiple high b-values. The above analysis assumes measurements with a single b-value. If data are collected with multiple b-values that are sensitive to the practical range of axon diameter in tissue, the lower and upper bounds of $S_{cylinder}$ (corresponding to upper bound and lower bound of axon diameter) become vectors $[\bar{\sigma}, S_{stick} - \bar{\sigma}]$. In this case, we can approximate the sensitivity range by finding the diameters that give minimal mean squared error (MSE) between their signals and signal bounds across all shells. For estimating upper bound of axon diameters, we use only shells of high b-values because data with lower b-values can be sensitive to infinitely large axons, and if included their signal contributions will dominate the calculation of MSE. Considering the three high b-shells in Figure 2 (B) (Figure 3 (A)) for ex vivo imaging ($b = 18.1, 25$ and $43 \text{ ms}/\mu\text{m}^2$), the sensitivity ranges are $[1.42, 10.5]$, $[1.70, 9.18]$, and $[1.94, 8.32] \mu\text{m}$ for SNR level of 100, 50 and 30 respectively.

3.2 Inspecting quality of fitting and MCMC samples

We introduced a two-stage MCMC fitting strategy for improving the fitting of axon diameter indices in ex vivo tissue by inspecting the quality of fit and MCMC samples (Gong et al., 2024b). Previous studies have used only the intra-axonal compartment with very few, ultra-high b-values ($\geq 20 \text{ ms}/\mu\text{m}^2$ for ex

vivo tissue) for axon diameter estimation. We use the multi-compartment model ‘ExCaliber’, taking into account that a nonnegligible and spatially varying dot signal is present in ex vivo tissue at high b-values and that it needs to be differentiated from the intra-axonal signals. We therefore model the full signal decay from a range of low and high b-values. The 5 free parameters in the ‘ExCaliber’ model are the axon diameter, the intra-axonal parallel diffusivity, the extra-cellular perpendicular diffusivity, and the intra-axonal and dot signal fraction. Parallel diffusivities in the intra-axonal and extra-cellular space are assumed to be equal to the intrinsic diffusivity.

We demonstrate this by simulating an example set of measurements. This is done by computing the forward model for ground-truth parameters typical of a WM voxel: axon diameter $da = 2 \mu\text{m}$, intra-axonal signal fraction $fia = 0.7$, dot signal fraction $fdot = 0.15$, parallel diffusivity $dpara = 0.6 \mu\text{m}^2/\text{ms}$ and perpendicular diffusivity $dperp = 0.6 * 0.3 \mu\text{m}^2/\text{ms}$. We added Gaussian-distributed noise to the signals to generate measurements at SNR =100. Figure 4 shows the quality of fit and posterior samples after the first and second MCMC run on these measurements. In the first stage, where all 5 tissue parameters were sampled, we found high uncertainty of estimated intra-axonal fractions. By fixing the parallel diffusivity and extra-cellular perpendicular diffusivity to their posterior means and sampling only the distributions of other 3 tissue parameters, , the second MCMC run achieved similar likelihood of measurements, lower parameter uncertainty for axon diameter and compartment signal fractions, and better quality of fit as evidenced by the fitting curve.

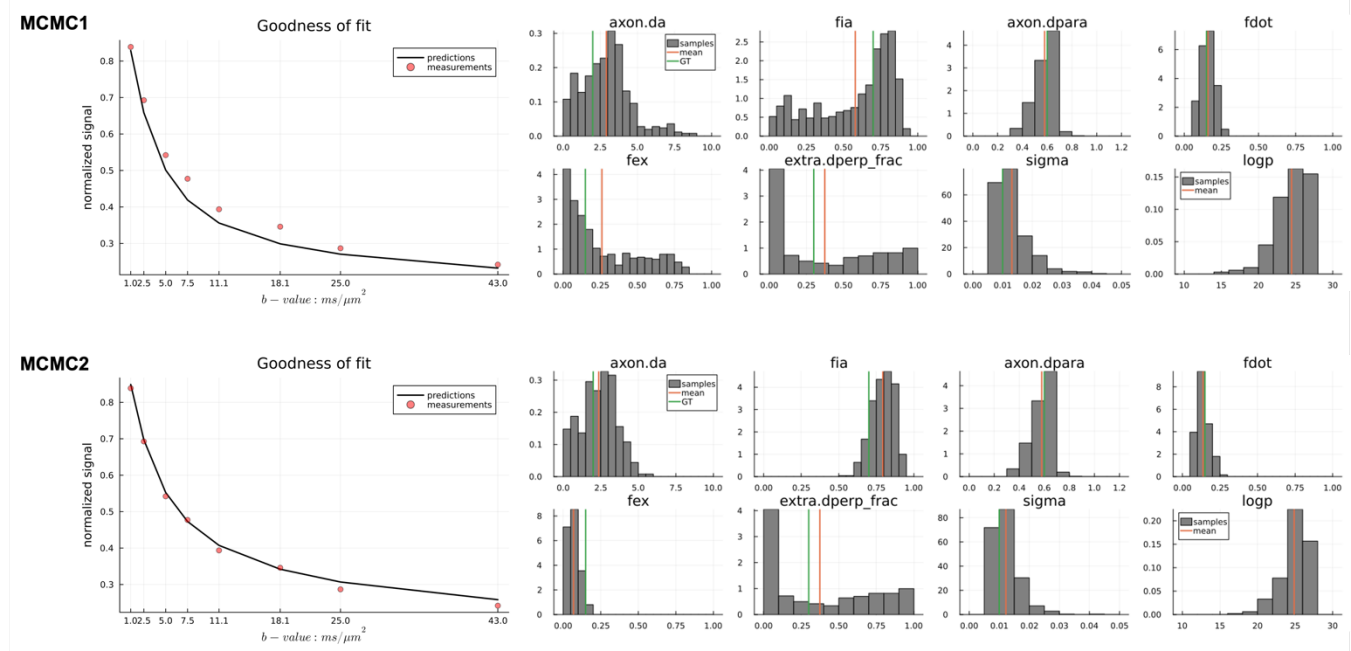


Figure 4. Fitting curves and posterior samples from the two MCMC runs of a two-stage MCMC fitting approach. We show the posterior distributions as histograms, with the mean estimates and ground truth (GT) tissue parameters indicated by green and orange lines, respectively. The parameters are the axon diameter (axon.da/ μm), the intra-axonal signal fraction (fia), the intra-axonal parallel diffusivity (axon.dpara/ $\mu\text{m}^2/\text{ms}$), the dot signal fraction (fdot), the extra-cellular signal fraction (fex), the extra-cellular perpendicular diffusivity represented as a fraction to the parallel diffusivity (extra.derp_frac),

the noise level (sigma), and the log likelihood of measurements (logp). The histograms are normalized so that the area in each histogram is one.

3.3 Evaluation of estimation accuracy and precision

Synthetic datasets with known ground truth parameters are essential for evaluating the accuracy and precision of microstructure model estimates for different data acquisition protocols. We demonstrate this approach for evaluating axon diameter estimation, by generating signals using the three-compartment tissue model ‘ExCaliber’ with axon diameters ranging from 1 μm to 10 μm at 1 μm intervals. This range of evaluation extends slightly beyond the sensitivity limits calculated from the Cylinder compartment in Section 3.1.

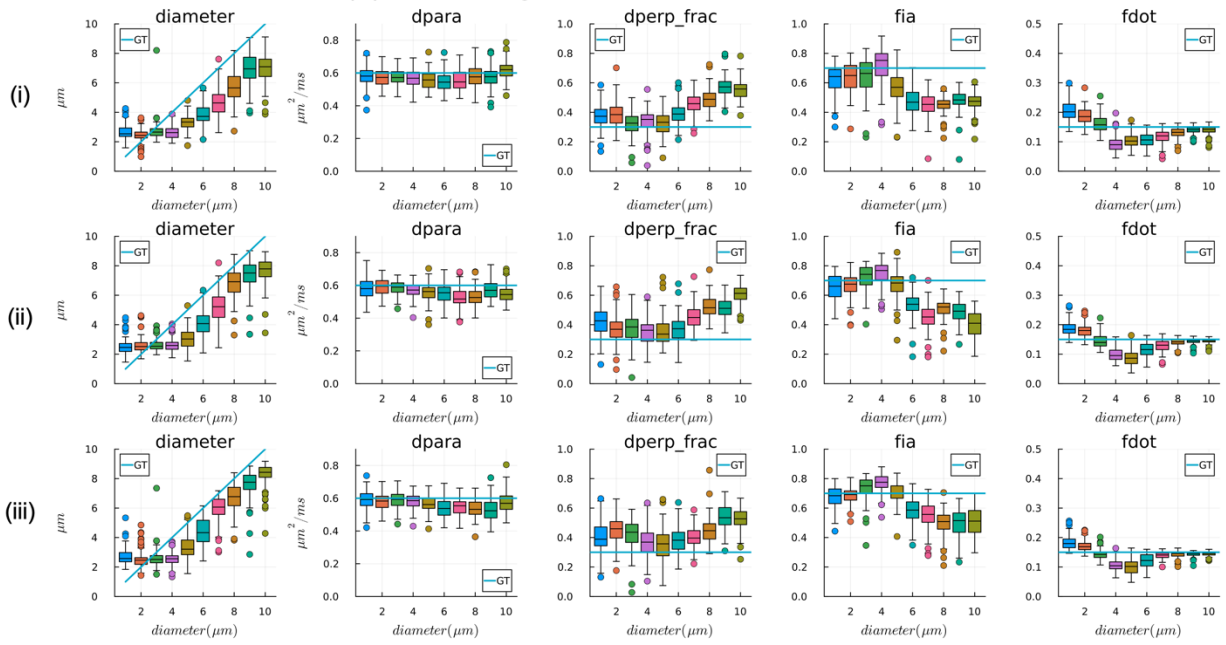
The tissue parameters chosen for the synthetic data were values typically observed in ex vivo WM tissue: intra-axonal signal fraction $f_{\text{ia}} = 0.7$, dot signal fraction $f_{\text{dot}} = 0.15$, extra-cellular signal fraction $f_{\text{ex}} = 0.15$, perpendicular diffusivity $d_{\text{para}} = 0.6 \mu\text{m}^2/\text{ms}$ and perpendicular diffusivity $d_{\text{perp}} = 0.6 * 0.3 \mu\text{m}^2/\text{ms}$. We tested three protocols with a single diffusion time and multiple b-values, where the maximum b-value was chosen to reach Gmax. The first had $\delta/\Delta = 9.6/12 \text{ ms}$ and $b = 1, 2.5, 5, 7.5, 11.1, 18.1, 25 \text{ ms}/\mu\text{m}^2$ (7 b-values total), the second had $\delta/\Delta = 11/15.192 \text{ ms}$ and an additional $b = 43 \text{ ms}/\mu\text{m}^2$ (8 b-values total), and the third had $\delta/\Delta = 11/21 \text{ ms}$ and an additional $b = 64 \text{ ms}/\mu\text{m}^2$ (9 b-values total). Gaussian-distributed noise was added to generate 100 realizations of noisy signals with SNR of 100 and 30. Figure 5 shows the estimated parameters using the two-stage approach in 3.2 from the 100 noise realizations as boxplots and the ground truth values as line plots.

Single diffusion time measurements. When compared to larger axons, the diameter estimates of smaller axons had higher precision and more accurate intra-axonal signal fractions. However, diameter estimates in the low range were biased in a way that made different diameters more difficult to discriminate. In comparison, the diameters and intra-axonal signal fractions of larger axons were always under-estimated, while the dot signal fractions were more accurate. Among the different diffusion times, the intermediate diffusion time of $\Delta = 15.2 \text{ ms}$ maintained a consistent trend of axon diameter estimates, even for axon diameters near the resolution limit calculated in section 3.1.

Comparison of the two SNR levels shows that the lower SNR (SNR = 30) decreased estimation precision for smaller axons but increased the discriminability of axon diameters in the low range. At this SNR, consistent trends were observed for the protocols with shorter diffusion times ($\Delta = 12$ and 15.2 ms), along with underestimation of intra-axonal fractions. These informative findings highlight the importance of such evaluations conveniently provided by the package.

Multiple diffusion times measurements. Including data with multiple diffusion times improved the accuracy of axon diameter estimation with better discriminability between smaller axons and lower biases and variances for larger axons, particularly at high SNR. However, at lower SNR, there was less to be gained by including multiple diffusion times vs. a single diffusion time (see Figure 5(B,i-ii) and Figure 6(B,i-ii)), as the differences between signals with different diffusion times were very small. In real datasets, we need to consider if the SNR is sufficient for the differences between signals acquired with different diffusion times to be significant. When using data from all the diffusion times for fitting, both the bias and variance decreased substantially.

(A) Data of single diffusion time, SNR = 100



(B) Data of single diffusion time, SNR = 30

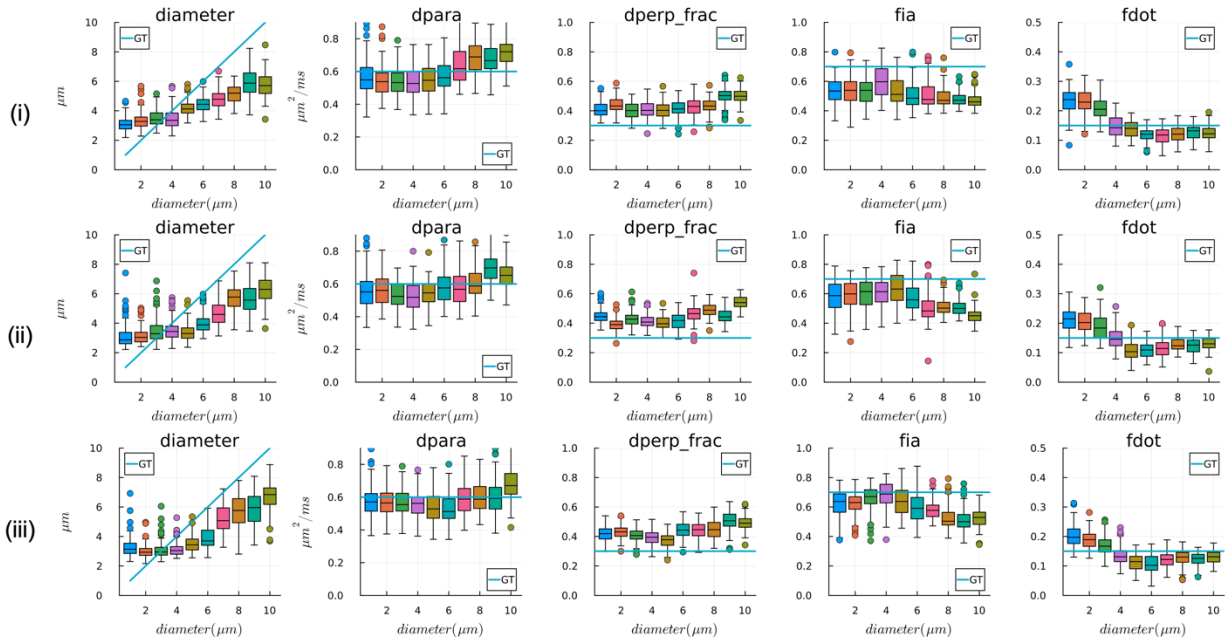


Figure 5. Estimates of axon diameters from single diffusion time data when (A) SNR = 100 and (B) SNR = 30. (i) Data generated with 7 values, $b_{\max} = 25 \text{ ms}/\mu\text{m}^2$ and $\delta/\Delta = 9.6/12 \text{ ms}$; (ii) Data generated with 8 b-values, $b_{\max} = 43 \text{ ms}/\mu\text{m}^2$ and $\delta/\Delta = 11/15.2 \text{ ms}$; (iii) Data generated with 9 b-values, $b_{\max} = 64 \text{ ms}/\mu\text{m}^2$ and $\delta/\Delta = 11/21 \text{ ms}$. Parameter estimates from 100 noise realizations are shown as boxplots and ground-truth (GT) parameter values are shown as line plots. The parameters are the axon diameter (diameter), the intra-axonal parallel diffusivity (dpara), the extra-cellular perpendicular diffusivity as a fraction to parallel diffusivity (dperp_frac), the intra-axonal signal fraction (fia), and the dot signal fraction (fdot).

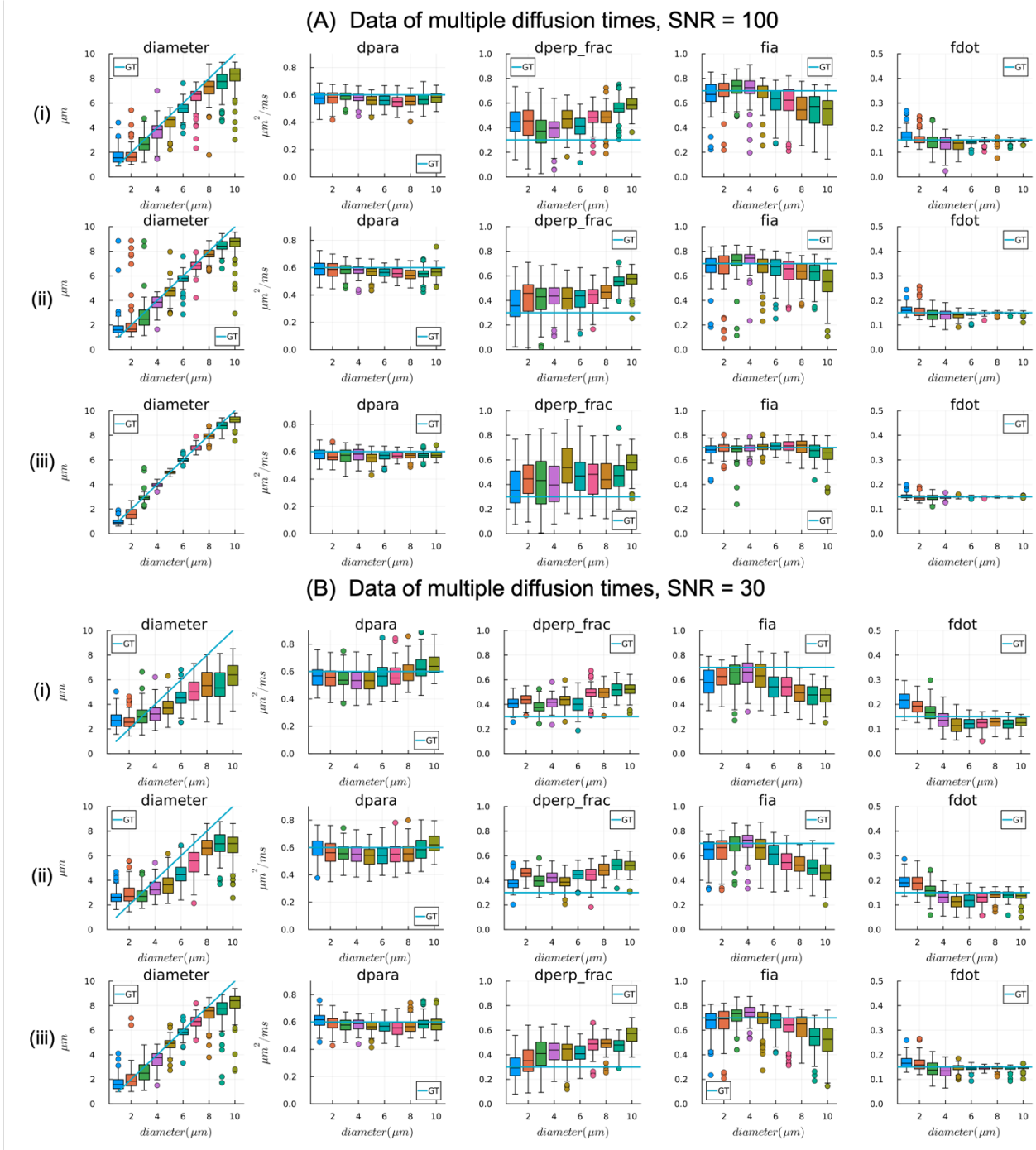


Figure 6. Estimates of axon diameter from multi-diffusion time data when (A) SNR = 100 and (B) SNR = 30. (i) Data combining two shorter diffusion times: $\delta/\Delta = 9.6/12$ ms and $\delta/\Delta = 11/15.2$ ms; (ii) Data combining two longer diffusion times $\delta/\Delta = 11/15.2$ ms and $\delta/\Delta = 11/21$ ms; (iii) Data combining all three diffusion times. Parameter estimates from 100 noise realizations are shown as boxplots and ground-truth parameter values are shown as line plots. The parameters are the axon diameter (diameter), the intra-axonal parallel diffusivity (dpara), the extra-cellular perpendicular diffusivity as a fraction to parallel diffusivity (dperp_frac), the intra-axonal signal fraction (fia), and the dot signal fraction (fdot).

4. Ongoing Work

This preprint reflects current progress on Microstructure.jl, while we are working on several improvements.

MCMC

Summary and diagnostic metrics from parameter posteriors. When using multi-threading to process an entire imaging dataset, the mean and standard deviation of the posterior samples are saved as parameter maps. Full posterior distributions are not stored due to memory constraints. However, the single-threaded '*mcmc*' function returns the full chain of samples, which can be used for detailed inspection of posteriors from specific voxel measurements or synthetic data. In future updates, we will save more summary and diagnostic metrics from posterior distributions when processing whole-brain datasets. These metrics are crucial for identifying parameter degeneracy and estimation ambiguity as highlighted by a prior study (Jallais and Palombo, 2023).

Optimized samplers for each microstructure model. We are evaluating the effects of different MCMC sampling parameters across various models in the package, with particular focus on diffusion-relaxometry models. Implementing shorter chains than those currently tested, as recommended by (Harms and Roebroeck, 2018) will reduce computation time for whole-brain datasets. Moreover, using a more informed initial guess as a starting point, rather than a random one, could potentially accelerate the sampling process. This initial guess can be provided for a whole-brain dataset with minimal additional computational cost by leveraging (potentially biased) neural-network estimators (Gong et al., 2023b).

Neural networks

Optimized training datasets for neural network estimator. For supervised learning, a training dataset contains pairs of training inputs \mathcal{S} (measurements) and training labels $\boldsymbol{\theta}$ (tissue parameters). Typical methods collect densely sampled MRI data from a few training subjects and derive "ground-truth" training labels from these data by using conventional optimization methods. This not only requires study/protocol-specific training data but can also introduce bias to the training labels due to inaccurate parameter fitting or model degeneracy. An alternative approach is to generate synthetic training datasets by computing the forward microstructure model $\mathcal{S}(\mathbf{b}, \mathbf{t}) = f(\mathbf{b}, \mathbf{t}; \boldsymbol{\theta})$ on ground-truth parameters. This can be used to generate training data for a wider range of ground-truth parameter values and imaging acquisition protocols.

The distributions of parameters in $\boldsymbol{\theta}$ is crucial for determining the training and estimation accuracy as the estimation errors are optimized across all the training samples. Previously, we have generated samples using prior distributions of $\boldsymbol{\theta}$ estimated from typical human brains. This allows us to synthesize dMRI signals with realistic structures for training convolutional neural networks (CNN) to estimate fiber orientation distribution (Lin et al., 2019). While priors including brain structure benefit CNN training, they introduce imbalanced distributions of parameters in $\boldsymbol{\theta}$ and result in biased estimates, particularly in regions where the true parameter values are underrepresented in the training sample. This issue was demonstrated in our diffusion kurtosis imaging study (Li et al., 2019) and highlighted in a simulation

study (Gyori et al., 2021). We will optimize the training datasets by excluding parameter degendered training samples (identified by MCMC) and optimizing parameter distributions in training dataset.

Data Statement

The package source code can be found at <https://github.com/Tinggong/Microstructure.jl>. The scripts that implement the use cases in the demonstration section can be found at <https://github.com/Tinggong/Microstructure.jl>. Tutorials are available on our documentation website at <https://tinggong.github.io/Microstructure.jl/dev/>.

Appendix

Table 1. Explanations of the arguments in ‘Sampler’ and ‘Noisemodel’ for MCMC sampling.

Sampler	Explanation
params	A tuple of strings containing the parameters in the model to sample; all the other model parameters that are not included will be fixed to the values specified when declaring the model object
prior_range	The prior range for each parameter in ‘params’; the ranges will be checked after drawing each sample
proposal	The proposal distributions used for drawing samples
paralinks	Links between parameters; a parameter that is not included in the “params” is associated with a parameter in the “params”; A tuple of pairs or empty tuple
nsamples	The total number of iterations in each run
burnin	The number of samples discarded in the beginning of the chain
thinning	The interval to draw independent samples after burnin
Noisemodel	Explanation
logpdf	The noise model used to estimate the log likelihood of measurements, including Gaussian or Rician noise models
sigma_start	The starting value of noise level sigma (standard deviation), either for the level of Gaussian noise or the level of Gaussian underlying the Rician
sigma_range	The prior range for sigma; the ranges will be checked after each sample drawing; the SNR level is reflected by 1/sigma
proposal	The proposal distributions used for drawing samples of sigma

Table 2. Explanation of arguments in ‘NetworkArg’ and ‘TrainingArg’ for building and training MLP models.

NetworkArg	Explanation
model	An object of any biophysical model. This is used as the forward model to generate training dataset.
protocol	The protocol is needed for generating training dataset along with the model object
params	Like MCMC sampler, these are the parameters in a model you want to estimate
paralinks	Links between parameters; a parameter that is not included in the “params” is associated with a parameter in the “params”; can be tuple of pairs or empty
tissuetype	In_vivo or ex_vivo; this is used to determine the scaling factor
sigma	The number of samples discarded in the beginning of the chain
noise_type	The interval to draw independent samples
hidden_layers	A tuple containing the number of units in each hidden layer; the number of layers is determined by the length
nsamples	The number of samples for generating training dataset
nin	The number of input channels
nout	The number of output channels
dropoutp	The dropout probability of the dropout layer
TrainingArg	Explanation
batchsize	An integer specifying the batch size during training
lossf	The loss function used for training
lr	Learning rate
epoch	The number of epochs for training
tv_split	Training and validation data split ratio; 0.2 means 20% for validation
patience	A tuple of two integers specifying the patience for training loss plateau and validation loss to increase

References

- Alexander, D.C., 2008. A General Framework for Experiment Design in Diffusion MRI and Its Application in Measuring Direct Tissue-Microstructure Features. *Magn Reson Med* 60, 439–448.
<https://doi.org/10.1002/mrm.21646>
- Alexander, D.C., Dyrby, T.B., Nilsson, M., Zhang, H., 2019. Imaging brain microstructure with diffusion MRI: practicality and applications. *NMR Biomed.* <https://doi.org/10.1002/nbm.3841>
- Alexander, D.C., Hubbard, P.L., Hall, M.G., Moore, E.A., Ptito, M., Parker, G.J.M., Dyrby, T.B., 2010. Orientationally invariant indices of axon diameter and density from diffusion MRI. *Neuroimage* 52, 1374–1389. <https://doi.org/10.1016/j.neuroimage.2010.05.043>
- Andersson, M., Pizzolato, M., Kjer, H.M., Skodborg, K.F., Lundell, H., Dyrby, T.B., 2022. Does powder averaging remove dispersion bias in diffusion MRI diameter estimates within real 3D axonal architectures? *Neuroimage* 248. <https://doi.org/10.1016/j.neuroimage.2021.118718>

- Assaf, Y., Basser, P.J., 2005. Composite hindered and restricted model of diffusion (CHARMED) MR imaging of the human brain. *Neuroimage* 27, 48–58.
<https://doi.org/10.1016/j.neuroimage.2005.03.042>
- Balinov, B., Jönsson, B., Linse, P., Söderman, O., 1993. The NMR Self-Diffusion Method Applied to Restricted Diffusion. Simulation of Echo Attenuation from Molecules in Spheres and between Planes. *J Magn Reson A* 104, 17–25. <https://doi.org/10.1006/JMRA.1993.1184>
- Behrens, T.E.J., Woolrich, M.W., Jenkinson, M., Johansen-Berg, H., Nunes, R.G., Clare, S., Matthews, P.M., Brady, J.M., Smith, S.M., 2003. Characterization and Propagation of Uncertainty in Diffusion-Weighted MR Imaging. *Magn Reson Med* 50, 1077–1088. <https://doi.org/10.1002/MRM.10609>
- Bezanson, J., Edelman, A., Karpinski, S., Shah, V.B., 2014. Julia: A Fresh Approach to Numerical Computing. *SIAM Review* 59, 65–98. <https://doi.org/10.1137/141000671>
- Callaghan, P.T., Jolley, K.W., Lelievre, J., 1979. Diffusion of water in the endosperm tissue of wheat grains as studied by pulsed field gradient nuclear magnetic resonance. *Biophys J* 28, 133.
[https://doi.org/10.1016/S0006-3495\(79\)85164-4](https://doi.org/10.1016/S0006-3495(79)85164-4)
- Coelho, S., Baete, S.H., Lemberskiy, G., Ades-Aron, B., Barrol, G., Veraart, J., Novikov, D.S., Fieremans, E., 2022. Reproducibility of the Standard Model of diffusion in white matter on clinical MRI systems. *Neuroimage* 257, 119290. <https://doi.org/10.1016/J.NEUROIMAGE.2022.119290>
- Cook, P.A., Bai, Y., Hall, M.G., Nedjati-Gilani, S., Seunarine, K.K., Alexander, D.C., 2005. Camino: Diffusion MRI reconstruction and processing.
- Daducci, A., Canales-Rodríguez, E.J., Zhang, H., Dyrby, T.B., Alexander, D.C., Thiran, J.P., 2015. Accelerated Microstructure Imaging via Convex Optimization (AMICO) from diffusion MRI data. *Neuroimage* 105, 32–44. <https://doi.org/10.1016/j.neuroimage.2014.10.026>
- de Almeida Martins, J.P., Nilsson, M., Lampinen, B., Palombo, M., While, P.T., Westin, C.F., Szczepankiewicz, F., 2021. Neural networks for parameter estimation in microstructural MRI: Application to a diffusion-relaxation model of white matter. *Neuroimage* 244.
<https://doi.org/10.1016/j.neuroimage.2021.118601>
- Dong, Z., Wang, F., Wald, L., Setsompop, K., 2022. SNR-efficient distortion-free diffusion relaxometry imaging using accelerated echo-train shifted echo-planar time-resolving imaging (ACE-EPTI). *Magn Reson Med* 88, 164–179. <https://doi.org/10.1002/MRM.29198>
- Fair, M.J., Liao, C., Manhard, M.K., Setsompop, K., 2021. Diffusion-PEPTIDE: Distortion- and blurring-free diffusion imaging with self-navigated motion-correction and relaxometry capabilities. *Magn Reson Med* 85, 2417–2433. <https://doi.org/10.1002/MRM.28579>
- Fan, Q., Nummenmaa, A., Witzel, T., Ohringer, N., Tian, Q., Setsompop, K., Klawiter, E.C., Rosen, B.R., Wald, L.L., Huang, S.Y., 2020. Axon diameter index estimation independent of fiber orientation distribution using high-gradient diffusion MRI. *Neuroimage* 222.
<https://doi.org/10.1016/j.neuroimage.2020.117197>
- Fick, R.H.J., Wassermann, D., Deriche, R., 2019. The Dmipy Toolbox: Diffusion MRI Multi-Compartment Modeling and Microstructure Recovery Made Easy. *Front Neuroinform* 13, 480105.
<https://doi.org/10.3389/FNINF.2019.00064/BIBTEX>
- Garyfallidis, E., Brett, M., Amirkhanian, B., Rokem, A., van der Walt, S., Descoteaux, M., Nimmo-Smith, I., 2014. Dipy, a library for the analysis of diffusion MRI data. *Front Neuroinform* 8, 71423.
<https://doi.org/10.3389/FNINF.2014.00008/BIBTEX>
- Gilks, W.R., Richardson, S., Spiegelhalter, D., 1995. Markov chain Monte Carlo in practice. CRC press.

- Gong, T., Dann, E., Maffei, C., Lee, H.-H., Lee, H., Bachevalier, J., Huang, S., Haber, S., Yendiki, A., 2023a. Neurodevelopment of soma and neurite density revealed by ultra-high gradient strength diffusion MRI, in: OHBM 2023 Annual Meeting. Montreal .
- Gong, T., Dann, E., Maffei, C., Lee, H.-H., Lee, H., Bachevalier, J., Huang, S., Haber, S., Yendiki, A., 2024a. Untangling grey matter microstructure development: insights from soma, neurite, and myelin imaging on macaques, in: OHBM 2024 Annual Meeting. Seoul.
- Gong, T., Fair, M.J., Setsompop, K., Zhang, H., 2022. Enabling compartment-specific T2 and T2* mapping with Diffusion-PEPTIDE imaging, in: ISMRM 2022 Annual Meeting. London.
- Gong, T., Grussu, F., Wheeler-Kingshott, C.A.M., Alexander, D.C., Zhang, H., 2023b. Machine-learning-informed parameter estimation improves the reliability of spinal cord diffusion MRI. arXiv preprint arXiv:2301.12294.
- Gong, T., He, H., Zhong, J., Zhang, H., 2021a. MTE-NODDI made practical with learning-based acquisition and parameter-estimation acceleration, in: ISMRM 2021 Annual Meeting.
- Gong, T., Maffei, C., Dann, E., Lee, H.-H., Lee, H., Augustinack, J.C., Huang, S.Y., Haber, S.N., Yendiki, A., 2024b. Interplay between MRI-based axon diameter and myelination estimates in macaque and human brain. arXiv preprint arXiv:2407.02227.
- Gong, T., Tax, C.M., Mancini, M., Jones, D.K., Zhang, H., Palombo, M., 2023c. Multi-TE SANDI: Quantifying compartmental T2 relaxation times in the grey matter, in: ISMRM 2023 Annual Meeting. Toronto.
- Gong, T., Tong, Q., He, H., Sun, Y., Zhong, J., Zhang, H., 2020. MTE-NODDI: Multi-TE NODDI for disentangling non-T2-weighted signal fractions from compartment-specific T2 relaxation times. Neuroimage 217. <https://doi.org/10.1016/j.neuroimage.2020.116906>
- Gong, T., Tong, Q., Li, Z., He, H., Zhang, H., Zhong, J., 2021b. Deep learning-based method for reducing residual motion effects in diffusion parameter estimation. Magn Reson Med 85, 2278–2293. <https://doi.org/10.1002/MRM.28544>
- Grussu, F., Battiston, M., Palombo, M., Schneider, T., Wheeler-Kingshott, C.A.M.G., Alexander, D.C., 2021. Deep Learning Model Fitting for Diffusion-Relaxometry: A Comparative Study. Math Vis 159–172. https://doi.org/10.1007/978-3-030-73018-5_13
- Gyori, N.G., Palombo, M., Clark, C.A., Zhang, H., Alexander, D.C., 2021. Training data distribution significantly impacts the estimation of tissue microstructure with machine learning. Magn Reson Med. <https://doi.org/10.1002/mrm.29014>
- Harms, R.L., Roebroeck, A., 2018. Robust and fast markov chain monte carlo sampling of diffusion MRI microstructure models. Front Neuroinform 12, 399549. <https://doi.org/10.3389/FNINF.2018.00097/BIBTEX>
- Hutter, J., Slator, P.J., Christiaens, D., Teixeira, R.P.A.G., Roberts, T., Jackson, L., Price, A.N., Malik, S., Hajnal, J. V., 2018. Integrated and efficient diffusion-relaxometry using ZEBRA. Sci Rep. <https://doi.org/10.1038/s41598-018-33463-2>
- Jallais, M., Palombo, M., 2023. \$\mu\$GUIDE: a framework for microstructure imaging via generalized uncertainty-driven inference using deep learning.
- Jelescu, I.O., de Skowronski, A., Geffroy, F., Palombo, M., Novikov, D.S., 2022. Neurite Exchange Imaging ((NEXI)): A minimal model of diffusion in gray matter with inter-compartment water exchange. Neuroimage 256. <https://doi.org/10.1016/j.neuroimage.2022.119277>
- Jespersen, S.N., Bjarkam, C.R., Nyengaard, J.R., Chakravarty, M.M., Hansen, B., Vosegaard, T., Østergaard, L., Yablonskiy, D., Nielsen, N.C., Vestergaard-Poulsen, P., 2010. Neurite density from

- magnetic resonance diffusion measurements at ultrahigh field: Comparison with light microscopy and electron microscopy. *Neuroimage* 49, 205–216.
<https://doi.org/10.1016/J.NEUROIMAGE.2009.08.053>
- Jespersen, S.N., Kroenke, C.D., Østergaard, L., Ackerman, J.J.H., Yablonskiy, D.A., 2007. Modeling dendrite density from magnetic resonance diffusion measurements. *Neuroimage* 34, 1473–1486.
<https://doi.org/10.1016/j.neuroimage.2006.10.037>
- Kaden, E., Kruggel, F., Alexander, D.C., 2016. Quantitative mapping of the per-axon diffusion coefficients in brain white matter. *Magn Reson Med* 75, 1752–1763.
<https://doi.org/10.1002/MRM.25734>
- Kroenke, C.D., Ackerman, J.J.H., Yablonskiy, D.A., 2004. On the nature of the NAA diffusion attenuated MR signal in the central nervous system. *Magn Reson Med* 52, 1052–1059.
<https://doi.org/10.1002/MRM.20260>
- Lampinen, B., Szczepankiewicz, F., Novén, M., van Westen, D., Hansson, O., Englund, E., Mårtensson, J., Westin, C.F., Nilsson, M., 2019. Searching for the neurite density with diffusion MRI: Challenges for biophysical modeling. *Hum Brain Mapp* 40, 2529–2545. <https://doi.org/10.1002/hbm.24542>
- Li, Z., Gong, T., Lin, Z., He, H., Tong, Q., Li, C., Sun, Y., Yu, F., Zhong, J., 2019. Fast and robust diffusion kurtosis parametric mapping using a three-dimensional convolutional neural network. *IEEE Access* 7. <https://doi.org/10.1109/ACCESS.2019.2919241>
- Lin, Z., Gong, T., Wang, K., Li, Z., He, H., Tong, Q., Yu, F., Zhong, J., 2019. Fast learning of fiber orientation distribution function for MR tractography using convolutional neural network. *Med Phys* 46. <https://doi.org/10.1002/mp.13555>
- Neuman, C.H., 1974. Spin echo of spins diffusing in a bounded medium. *J Chem Phys* 4508–4511.
<https://doi.org/10.1063/1.1680931>
- Nilsson, M., Lasić, S., Drobnjak, I., Topgaard, D., Westin, C.F., 2017. Resolution limit of cylinder diameter estimation by diffusion MRI: The impact of gradient waveform and orientation dispersion. *NMR Biomed* 30. <https://doi.org/10.1002/NBM.3711>
- Novikov, D.S., Fieremans, E., Jespersen, S.N., Kiselev, V.G., 2019. Quantifying brain microstructure with diffusion MRI: Theory and parameter estimation. *NMR Biomed*.
<https://doi.org/10.1002/nbm.3998>
- Novikov, D.S., Veraart, J., Jelescu, I.O., Fieremans, E., 2018. Rotationally-invariant mapping of scalar and orientational metrics of neuronal microstructure with diffusion MRI. *Neuroimage* 174, 518–538. <https://doi.org/10.1016/J.NEUROIMAGE.2018.03.006>
- Olesen, J.L., Østergaard, L., Shemesh, N., Jespersen, S.N., 2022. Diffusion time dependence, power-law scaling, and exchange in gray matter. *Neuroimage* 251.
<https://doi.org/10.1016/j.neuroimage.2022.118976>
- Palombo, M., Ianus, A., Guerreri, M., Nunes, D., Alexander, D.C., Shemesh, N., Zhang, H., 2020. SANDI: A compartment-based model for non-invasive apparent soma and neurite imaging by diffusion MRI. *Neuroimage* 215. <https://doi.org/10.1016/j.neuroimage.2020.116835>
- Palombo, M., Valindria, V., Singh, S., Chiou, E., Giganti, F., Pye, H., Whitaker, H.C., Atkinson, D., Punwani, S., Alexander, D.C., Panagiotaki, E., 2023. Joint estimation of relaxation and diffusion tissue parameters for prostate cancer with relaxation-VERDICT MRI. *Scientific Reports* 2023 13:1 13, 1–13. <https://doi.org/10.1038/s41598-023-30182-1>

- Panagiotaki, E., Schneider, T., Siow, B., Hall, M.G., Lythgoe, M.F., Alexander, D.C., 2012. Compartment models of the diffusion MR signal in brain white matter: A taxonomy and comparison. *Neuroimage* 59, 2241–2254. <https://doi.org/10.1016/j.neuroimage.2011.09.081>
- Panagiotaki, E., Walker-Samuel, S., Siow, B., Johnson, S.P., Rajkumar, V., Pedley, R.B., Lythgoe, M.F., Alexander, D.C., 2014. Noninvasive quantification of solid tumor microstructure using VERDICT MRI. *Cancer Res* 74, 1902–1912. <https://doi.org/10.1158/0008-5472.CAN-13-2511/651164/AM/NON-INVASIVE-QUANTIFICATION-OF-SOLID-TUMOR>
- Slator, P.J., Palombo, M., Miller, K.L., Westin, C.F., Laun, F., Kim, D., Haldar, J.P., Benjamini, D., Lemberskiy, G., de Almeida Martins, J.P., Hutter, J., 2021. Combined diffusion-relaxometry microstructure imaging: Current status and future prospects. *Magn Reson Med.* <https://doi.org/10.1002/mrm.28963>
- Tariq, M., Schneider, T., Alexander, D.C., Gandini Wheeler-Kingshott, C.A., Zhang, H., 2016. Bingham-NODDI: Mapping anisotropic orientation dispersion of neurites using diffusion MRI. *Neuroimage* 133, 207–223. <https://doi.org/10.1016/j.neuroimage.2016.01.046>
- Tournier, J.D., Smith, R., Raffelt, D., Tabbara, R., Dhollander, T., Pietsch, M., Christiaens, D., Jeurissen, B., Yeh, C.H., Connelly, A., 2019. MRtrix3: A fast, flexible and open software framework for medical image processing and visualisation. *Neuroimage* 202, 116137. <https://doi.org/10.1016/J.NEUROIMAGE.2019.116137>
- Van Gelderen, P., Des Pres, D., Van Zijl, P.C.M., Moonen, C.T.W., 1994. Evaluation of Restricted Diffusion in Cylinders. Phosphocreatine in Rabbit Leg Muscle. *J Magn Reson B* 103, 255–260. <https://doi.org/10.1006/JMRB.1994.1038>
- Veraart, J., Novikov, D.S., Fieremans, E., 2017. TE dependent Diffusion Imaging (TEdDI) distinguishes between compartmental T 2 relaxation times. <https://doi.org/10.1016/j.neuroimage.2017.09.030>
- Wang, F., Dong, Z., Reese, T.G., Bilgic, B., Katherine Manhard, M., Chen, J., Polimeni, J.R., Wald, L.L., Setsompop, K., 2019. Echo Planar Time-resolved Imaging (EPTI). *Magn Reson Med* 81, 3599. <https://doi.org/10.1002/MMR.27673>
- Zhang, H., Hubbard, P.L., Parker, G.J.M., Alexander, D.C., 2011. Axon diameter mapping in the presence of orientation dispersion with diffusion MRI. *Neuroimage* 56, 1301–1315. <https://doi.org/10.1016/j.neuroimage.2011.01.084>
- Zhang, H., Schneider, T., Wheeler-Kingshott, C.A., Alexander, D.C., 2012. NODDI: Practical in vivo neurite orientation dispersion and density imaging of the human brain. *Neuroimage* 61, 1000–1016. <https://doi.org/10.1016/j.neuroimage.2012.03.072>